Near-inertial waves and geostrophic turbulence

Jim Thomas[1,*] and S. Arun[2]

[1]*Department of Mathematics, University of North Carolina at Chapel Hill,
Chapel Hill, North Carolina 27599, USA*
[2]*Department of Aerospace Engineering, Indian Institute of Technology Madras,
Chennai, Tamil Nadu 600036, India*

Wind-forced near-inertial waves form a high-energy wave component in the upper ocean. The weakly dispersive nature of these large horizontal and small vertical scale waves make them suitable candidates for energetic interactions with mesoscale balanced flows. We take advantage of an idealized two-vertical-mode system obtained by projecting the hydrostatic Boussinesq equations onto the barotropic and a single high baroclinic mode to examine wave-balanced flow interactions. Our detailed analysis using results of freely evolving numerical simulations demonstrate how the well established two-mode quasigeostrophic turbulence phenomenology changes in the presence of high-energy near-inertial waves. In the absence of waves, the barotropic flow, which contains most of the balanced energy, undergoes an inverse energy cascade resulting in the formation of large-scale coherent vortices. In contrast, high-energy near-inertial waves transfer energy to the barotropic flow, facilitating a forward energy cascade of the balanced flow. The balanced flow in turn assists in the forward energy cascade of the wave field, which transforms the wave field from low-frequency near-inertial waves to high-frequency inertia-gravity waves. Given that the idealized model we employ is two-dimensional, the forward energy cascade of wave and balanced flow is an unexpected and intriguing feature.

I. INTRODUCTION

Near-inertial waves (NIWs), generated by atmospheric winds and storms, form a ubiquitous wave field in the upper ocean. With roughly 0.3–0.7 TW being input into the near-inertial frequency band by the atmospheric activity [1,2], understanding the dynamics of NIWs—specifically the formation of small-scale waves from initially large-scale waves, vertical propagation from the mixed layer into the thermocline, and the eventual wave breaking and three-dimensional turbulent mixing—is key to quantifying oceanic interior energy pathways and localized diapycnal mixing. The large horizontal and small vertical scales of NIWs makes them weakly dispersive, allowing them to remain in a specific region longer than other rapidly propagating internal gravity waves, such as low baroclinic mode internal tides, for example. This weakly dispersive nature makes NIWs suitable candidates for energy exchanges with slow evolving geostrophic balanced flows in the upper ocean, inspiring a wide variety of studies that have examined NIW-balanced flow interactions.

The NIW-balanced flow investigations of the past may be broadly divided into those focusing on Ro ∼ 1 regime and Ro ≪ 1 regime, Ro being the Rossby number of the flow. In the Ro ∼ 1 regime, Gertz and Straub [3] and Taylor and Straub [4] examined NIW-balanced flow interactions using forced-dissipative large-scale ocean model simulations. Gertz and Straub found that at large scales NIWs transferred energy to the balanced flow in small balance-to-wave energy regions

---

*jimthomas.edu@gmail.com

014801-1

while Taylor and Straub report that externally forced NIWs could be a potential sink for the mesoscale balanced flow energy. Barkan *et al.* [5] used forced-dissipative simulations to point out that NIWs not only extracted energy from the balanced flow but also assisted in transfer of balanced energy from mesoscales to submesoscales. On a different route, multiple studies have examined interactions between NIWs and balanced ocean fronts. Among these, Thomas and Taylor [6] describes an interaction where NIWs, aided by parametric subharmonic instability, transfers energy to the baroclinic balanced currents. Along the same lines, Nagai *et al.* [7] found that spontaneously generated NIWs transferred energy to the Kuroshio front; this also being a case where waves transferred energy to the balanced flow. However, Thomas [8] and Shakespeare and Hogg [9] describe front-wave interactions resulting in waves gaining or losing energy to the mean flow, depending on the relative alignment of the two fields.

The above discussion brings out the lack of a unified point of view on the direction of energy transfer between NIWs and balanced flows. Of course, given that the equations governing the dynamics of rotating stratified fluid flows are not known to favor any preferred energy flow pathways, the lack of consensus on energy exchange is not much of a surprise. Each of the previously described work is based on a specific configuration, making their results depend on the detailed set up. Furthermore, in the regime $Ro \sim 1$, wave-balanced flow decomposition is nontrivial, since the linear and the nonlinear terms in the equations of motion are comparable in this regime. The results for energy transfer pathways therefore depends on the strict definition of wave and balanced flow used in the specific set up, contributing to the lack of a generic energy flow direction between wave and balanced flow. In contrast, the wave-balanced flow decomposition is much more transparent in the asymptotic regime $Ro \ll 1$. The decomposition in this regime can take advantage of the linear equations, since the linear terms are asymptotically larger than the nonlinear terms. Therefore without any ambiguity one can identify linear waves and a component that is orthogonal to it—the geostrophic balanced flow. The orthogonality of wave and balanced flow based on the linear equations imply that one can split quadratic invariants, such as energy, for example, exactly into two parts: a part that is entirely due to waves and the remaining due to balanced flow alone (see, for example, Deusebio *et al.* [10], Herbert *et al.* [11], and Waite [12]). This provides a clear means of diagnosing wave-balance energy exchanges.

In the $Ro \ll 1$ regime, multiple studies have focused on deriving asymptotic models to examine NIW-balanced flow energy exchanges. Young and Ben Jelloul [13] (YBJ hereafter) derived an approximate asymptotic model for the evolution of NIWs in a mesoscale balanced flow field in the limit of small amplitude waves. Recently Xie and Vanneste [14] (XV hereafter) developed a coupled model, where the wave equation evolves according to the approximate YBJ equation, while the balanced flow evolves according to a "quasigeostrophic like" equation, with nonlinear wave interaction terms being part of it. XV used this approximate asymptotic model to argue that NIWs directly extract energy from the balanced flow. Wagner and Young [15] (WY hereafter) extended XV's model, by adding a weak second harmonic inertial wave component (here "weak" means that the second harmonic wave field's magnitude was asymptotically smaller than that of the first harmonic wave). The second harmonic wave being weak does not directly affect the balanced flow in their model, implying that the asymptotic model of WY has the same balanced flow evolution equation as XV. Nevertheless, WY used numerical simulations in a two-dimensional *x-z* plane to demonstrate that the scattering of NIWs by the balanced flow can generate second harmonic inertial waves. More recently, Rocha *et al.* [16] (RWY hereafter) projected the approximate asymptotic model of XV onto the barotropic and a single plane wave in the vertical, resulting in a reduced two-dimensional version of XV's model in the *x-y* plane. RWY simulated this reduced two-dimensional model to argue that NIWs could extract energy from a time evolving balanced flow.

In this work we examine energy exchanges between NIWs and balanced flows in the $Ro \ll 1$ regime by taking advantage of an idealized two-dimensional model obtained by projecting the hydrostatic Boussinesq equations onto the barotropic and a single high-baroclinic mode. Our approach is therefore complementary to that of RWY, who examined NIW-balanced flow energy exchanges in a two-dimensional model obtained by a Galerkin truncation of the asymptotic model

of XV. Notably, the key difference here is that we perform a Galerkin truncation of the parent model—the hydrostatic Boussinesq equations—onto the barotropic and a single high baroclinic mode. This means that our idealized two-dimensional model can form the starting point from which coupled NIW-balanced flow asymptotic models such as those mentioned above can be derived. For instance, Danioux *et al.* [17] and Thomas *et al.* [18] derived the YBJ equation from the same high baroclinic mode equations that we use here. Therefore, our model, while being idealized due to its two-dimensional nature, contains richer dynamics compared to the approximate asymptotic models mentioned before.

Since we use a reduced yet nonasymptotic model, in the hierarchy of NIW-balanced flow studies described earlier, our investigation falls between those that have used asymptotic models and those that have used more complex three-dimensional models. Of course, we note that our reduced model that allows only two vertical modes is expected to miss significant three-dimensional features. Nevertheless, the idealization allows us to explore the NIW-balanced flow interactions in great detail without making additional asymptotic approximations. The present investigation takes a similar approach as that of Thomas and Yamada [19] (TY hereafter) who examined the energy exchanges between first baroclinic mode internal gravity waves and balanced flows. Complementary to the results discussed in TY, in this paper we will explain how high baroclinic mode NIWs modify the two-mode quasigeostrophic turbulence phenomenology. The plan for the paper is as follows: we discuss the model and its features in Sec. II, present results based on numerical simulations examining NIW-balanced flow interactions in Sec. III, and conclude with discussions of our findings in a broader context in Sec. IV.

II. THE MODEL AND ITS FEATURES

The hydrostatic Bousinesq equations on the "f-plane" are

$$\frac{\partial \boldsymbol{v}}{\partial t} + \boldsymbol{f} \times \boldsymbol{v} + \boldsymbol{\nabla} p + \boldsymbol{v} \cdot \boldsymbol{\nabla} \boldsymbol{v} + w \frac{\partial \boldsymbol{v}}{\partial z} = 0, \tag{1a}$$

$$\frac{\partial b}{\partial t} + N^2 w + \boldsymbol{v} \cdot \boldsymbol{\nabla} b + w \frac{\partial b}{\partial z} = 0, \tag{1b}$$

$$\frac{\partial p}{\partial z} = b, \tag{1c}$$

$$\boldsymbol{\nabla} \cdot \boldsymbol{v} + \frac{\partial w}{\partial z} = 0, \tag{1d}$$

where $\boldsymbol{v} = (u, v)$ and w are the horizontal and vertical velocities, respectively, b is the buoyancy, p is the pressure, $\boldsymbol{f} = f\hat{z}$ with f being the constant rotation rate and $\hat{z}$ being the unit vector in the z-direction, and N is the constant buoyancy frequency.

We expand all variables in terms of the barotropic and the nth baroclinic mode as

$$(\boldsymbol{v}, p) = (\boldsymbol{v}_T, p_T) + \sqrt{2}(\boldsymbol{v}_C, p_C) \cos\left(\frac{n\pi z}{H}\right) \tag{2a}$$

$$(w, b) = \sqrt{2}(w_C, b_C) \sin\left(\frac{n\pi z}{H}\right) \tag{2b}$$

Using the expansion Eqs. (2) and projecting Eqs. (1) on the two vertical modes gives us

$$\frac{\partial \boldsymbol{v}_T}{\partial t} + \boldsymbol{f} \times \boldsymbol{v}_T + \boldsymbol{\nabla} p_T + \boldsymbol{v}_T \cdot \boldsymbol{\nabla} \boldsymbol{v}_T + \boldsymbol{v}_C \cdot \boldsymbol{\nabla} \boldsymbol{v}_C + (\boldsymbol{\nabla} \cdot \boldsymbol{v}_C)\boldsymbol{v}_C = 0, \tag{3a}$$

$$\boldsymbol{\nabla} \cdot \boldsymbol{v}_T = 0, \tag{3b}$$

$$\frac{\partial \boldsymbol{v}_C}{\partial t} + \boldsymbol{f} \times \boldsymbol{v}_C + \boldsymbol{\nabla} p_C + (\boldsymbol{v}_T \cdot \boldsymbol{\nabla} \boldsymbol{v}_C + \boldsymbol{v}_C \cdot \boldsymbol{\nabla} \boldsymbol{v}_T) = 0, \tag{3c}$$

$$\frac{\partial p_C}{\partial t} + \left(\frac{NH}{n\pi}\right)^2 \boldsymbol{\nabla} \cdot \boldsymbol{v}_C + \boldsymbol{v}_T \cdot \boldsymbol{\nabla} p_C = 0. \tag{3d}$$

We nondimensionalize variables as

$$t \to t/f, \quad \boldsymbol{x} \to L\,\boldsymbol{x}, \quad (\boldsymbol{v}_T, \boldsymbol{v}_C) \to U(\boldsymbol{v}_T, \boldsymbol{v}_C), \quad (p_T, p_C) \to fUL(p_T, p_C). \qquad (4)$$

In the above scaling, time was nondimensionalized by the inertial timescale, $1/f$, while the length of the domain, L, was used to scale spatial coordinates x and y. U above is a scale for velocity, which may be considered to be the largest magnitude of the initial velocity prescribed in our freely evolving simulations. The scale for pressure was chosen such that the Coriolis term balances the pressure gradient term, i.e., $\boldsymbol{f} \times \boldsymbol{v} \sim \nabla p$.

Using Eq. (4) to nondimensionalize Eqs. (3) gives us

$$\frac{\partial \boldsymbol{v}_T}{\partial t} + \hat{\boldsymbol{z}} \times \boldsymbol{v}_T + \nabla p_T + \mathrm{Ro}[\boldsymbol{v}_T \cdot \nabla \boldsymbol{v}_T + \boldsymbol{v}_C \cdot \nabla \boldsymbol{v}_C + (\nabla \cdot \boldsymbol{v}_C)\boldsymbol{v}_C] = 0, \qquad (5a)$$

$$\nabla \cdot \boldsymbol{v}_T = 0, \qquad (5b)$$

$$\frac{\partial \boldsymbol{v}_C}{\partial t} + \hat{\boldsymbol{z}} \times \boldsymbol{v}_C + \nabla p_C + \mathrm{Ro}(\boldsymbol{v}_T \cdot \nabla \boldsymbol{v}_C + \boldsymbol{v}_C \cdot \nabla \boldsymbol{v}_T) = 0, \qquad (5c)$$

$$\frac{\partial p_C}{\partial t} + \mathrm{Bu}\nabla \cdot \boldsymbol{v}_C + \mathrm{Ro}(\boldsymbol{v}_T \cdot \nabla p_C) = 0, \qquad (5d)$$

where the Burger number, $\mathrm{Bu} = (NH/n\pi fL)^2$ and $\mathrm{Ro} = U/fL$ is the Rossby number. We rescale baroclinic pressure as $p_C \to \mathrm{Bu}\,p_C$ and rewrite the barotropic mode's equation by taking the curl of (5a) and defining $\zeta_T = \nabla \times \boldsymbol{v}_T$ to get

$$\frac{\partial \zeta_T}{\partial t} + \mathrm{Ro}\nabla \times [\boldsymbol{v}_T \cdot \nabla \boldsymbol{v}_T + \boldsymbol{v}_C \cdot \nabla \boldsymbol{v}_C + (\nabla \cdot \boldsymbol{v}_C)\boldsymbol{v}_C] = 0, \qquad (6a)$$

$$\frac{\partial \boldsymbol{v}_C}{\partial t} + \hat{\boldsymbol{z}} \times \boldsymbol{v}_C + \mathrm{Bu}\nabla p_C + \mathrm{Ro}(\boldsymbol{v}_T \cdot \nabla \boldsymbol{v}_C + \boldsymbol{v}_C \cdot \nabla \boldsymbol{v}_T) = 0, \qquad (6b)$$

$$\frac{\partial p_C}{\partial t} + \nabla \cdot \boldsymbol{v}_C + \mathrm{Ro}(\boldsymbol{v}_T \cdot \nabla p_C) = 0. \qquad (6c)$$

Equations (6) is the reduced model we will use for our investigation. Galerkin truncated models with two vertical modes, such as Eqs. (6), have been used for multiple idealized studies in the past. Examples include Frierson *et al.* [20] studying atmospheric convective processes, Benavides and Alexakis [21] examining the dynamics of thin fluid layers and associated turbulent energy flow pathways, and TY investigating energetic interactions between balanced flows and low mode internal tides in the ocean. The model used by TY consisted of the barotropic and the first baroclinic mode, which is a special case of Eqs. (6) for $n = 1$. In contrast, in this work we will examine interactions between high baroclinic mode NIWs and balanced flow. The baroclinic mode in our study is therefore a high mode that contains NIWs and we are set in the regime $n \gg 1$ so that $\mathrm{Bu} \ll 1$.

A. The wave-balance decomposition

We set $\mathrm{Ro} = 0$ in Eqs. (6) to obtain the linear equations:

$$\frac{\partial \zeta_T}{\partial t} = 0, \qquad (7a)$$

$$\frac{\partial \boldsymbol{v}_C}{\partial t} + \hat{\boldsymbol{z}} \times \boldsymbol{v}_C + \mathrm{Bu}\nabla p_C = 0, \qquad (7b)$$

$$\frac{\partial p_C}{\partial t} + \nabla \cdot \boldsymbol{v}_C = 0. \qquad (7c)$$

The barotropic mode (whose vorticity is ζ_T) is in geostrophic balance and has no linear time evolution, as is clear from Eq. (7a). However, the baroclinic mode, whose evolution is captured

by Eqs. (7b) and (7c)—equations identical to linear rotating shallow water equations—consists of a linear combination of a geostrophic balanced component and a gravity wave component, which we denote with subscripts G and W hereafter. The G-mode satisfy

$$\hat{z} \times \boldsymbol{v}_G + \mathrm{Bu}\boldsymbol{\nabla} p_G = 0, \tag{8a}$$

$$\boldsymbol{\nabla} \cdot \boldsymbol{v}_G = 0, \tag{8b}$$

and the W-mode satisfy

$$\frac{\partial \boldsymbol{v}_W}{\partial t} + \hat{z} \times \boldsymbol{v}_W + \mathrm{Bu}\boldsymbol{\nabla} p_W = 0, \tag{9a}$$

$$\frac{\partial p_W}{\partial t} + \boldsymbol{\nabla} \cdot \boldsymbol{v}_W = 0. \tag{9b}$$

The wave equations given in Eqs. (9), which are identical to linear rotating shallow water wave equations, captures the dynamics of a wide spectrum of waves with dispersion relationship: $\omega = \sqrt{1 + \mathrm{Bu}\,k^2}$. Given that our study is based in the parameter regime $\mathrm{Bu} \ll 1$, wave modes that satisfy $k \sim 1$ would qualify as NIWs, since for these waves $\mathrm{Bu}\,k^2 \ll 1 \Rightarrow \omega \sim 1$. In contrast, wave modes that satisfy $k \gg 1$ such that $\mathrm{Bu}\,k^2 \gg 1$ will have frequencies $\omega \gg 1$ and form high-frequency inertia-gravity waves. Therefore the W-component in the reduced model Eq. (6) can in general contain both low-frequency NIWs and high-frequency inertia-gravity waves, although we will examine initial value problems where the wave field is initialized as NIWs.

The reduced model Eqs. (6) conserves the sum of the energies of the three components, T, G, and W as

$$\frac{d}{dt} \iint \left(\frac{1}{2}\boldsymbol{v}_T^2 + \frac{1}{2}\boldsymbol{v}_W^2 + \frac{1}{2}\mathrm{Bu}\,p_W^2 + \frac{1}{2}\boldsymbol{v}_G^2 + \frac{1}{2}\mathrm{Bu}\,p_G^2 \right)dxdy = 0. \tag{10}$$

The model Eqs. (6) is therefore a complete, albeit idealized, reduced model that can capture the coupled evolution of waves and the balanced flow without relying on asymptotic approximations. The three components of the model Eqs. (6) discussed so far are schematically shown in Fig. 1.

B. A reduction of the model

We will now examine a reduction of the model, Eqs. (6). Consider the reduction that ignores the waves in the baroclinic mode. In this case we are left with the two balanced modes: T and G. To derive an asymptotic model that governs their coupled evolution, we leave out the waves and restrict the baroclinic fields to geostrophic balanced fields, i.e., $\boldsymbol{v}_C = \boldsymbol{v}_G$ and $p_C = p_G$ such that $\boldsymbol{v}_G = \mathrm{Bu}\,\hat{z} \times \boldsymbol{\nabla} p_G$. Using these in Eqs. (6), we get

$$\frac{\partial \zeta_T}{\partial t} + \mathrm{Ro}(\boldsymbol{v}_T \cdot \boldsymbol{\nabla}\zeta_T + \boldsymbol{v}_G \cdot \boldsymbol{\nabla}\zeta_G) = 0, \tag{11a}$$

$$\frac{\partial \zeta_G}{\partial t} + \mathrm{Ro}(\boldsymbol{v}_G \cdot \boldsymbol{\nabla}\zeta_T + \boldsymbol{v}_T \cdot \boldsymbol{\nabla}\zeta_G) = 0, \tag{11b}$$

$$\frac{\partial p_G}{\partial t} + \mathrm{Ro}(\boldsymbol{v}_T \cdot \boldsymbol{\nabla} p_G) = 0, \tag{11c}$$

where Eq. (11b) was obtained by taking the curl of Eq. (6b). Subtracting Eq. (11c) from Eq. (11b) and setting $p_G = \psi_G$, $\zeta_G = \mathrm{Bu}\Delta\psi_G$, and $\zeta_T = \Delta\psi_T$, we get the quasigeostrophic (QG) equations for the evolution of barotropic and baroclinic balanced flow as

$$\frac{\partial}{\partial t}\Delta\psi_T + \mathrm{Ro}\partial[\psi_T, \Delta\psi_T] + \mathrm{Ro}\partial[\psi_G, (\mathrm{Bu}\Delta - 1)\psi_G] = 0, \tag{12a}$$

$$\frac{\partial}{\partial t}(\mathrm{Bu}\Delta - 1)\psi_G + \mathrm{Ro}\partial[\psi_T, (\mathrm{Bu}\Delta - 1)\psi_G] + \mathrm{Ro}\partial[\psi_G, \Delta\psi_T] = 0, \tag{12b}$$
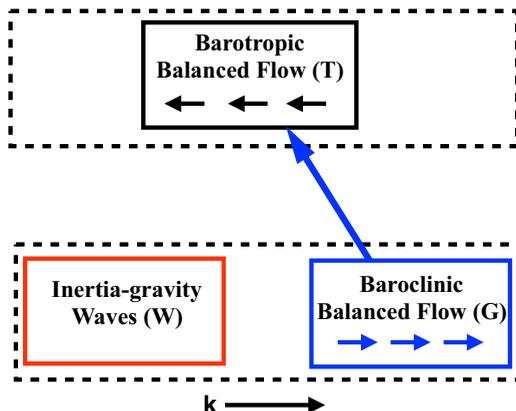
FIG. 1. Schematic showing the three components of the model, Eqs. (6). The barotropic mode (denoted by T) is balanced with no linear dynamics while the baroclinic mode consists of inertia-gravity waves (denoted by W) and a balanced component (denoted by G). In the absence of waves, the two-mode QG Eqs. (12) describes the interactions between the G and the T modes. In two-mode QG turbulence, the barotropic flow exhibits an inverse energy cascade (shown by small leftward pointing black arrows in the T box), while the baroclinic balanced flow exhibits a forward energy cascade (shown by small rightward pointing blue arrows in the G box). (Notice that the wavenumbers, k, increases towards right, as shown by the long horizontal black arrow at the bottom). Overall, the baroclinc flow loses energy to the barotropic flow in two-mode QG turbulence, as indicated by the long blue arrow connecting the T and G boxes. In this study we will examine how high baroclinic mode waves (indicated by the red box above), which are initially NIWs, can modify QG turbulence phenomenology.

where $\partial[f, g] = f_x g_y - f_y g_x$ is the Jacobian. Equations (12) are the two-mode QG equations for the coupled evolution of the barotropic and the nth baroclinic mode. We note that Eq. (12) could have been obtained by truncating the fully three-dimensional QG equation (see [22]) onto the barotropic and the nth baroclinic mode.

We simulated Eq. (6) in the parameter regimes corresponding to the above reduction, completely devoid of waves at $t = 0$. The numerical simulations presented here and later in this paper used a dealiased pseudospectral code. Although Eqs. (6) are inviscid, we added hyperviscous terms: $\nu \Delta^8 \zeta_T$, $\nu \Delta^8 \boldsymbol{v}_C$, and $\nu \Delta^8 p_C$ to the right-hand sides of Eqs. (6a)–(6c), respectively, to prevent accumulation of energy at the grid scale. We used a resolution of 384^2 (giving us a maximum wavenumber of $k_{\max} = 128$ in k_x and k_y directions after dealiazing) and $\nu = 2.4 \times 10^{-34}$ for the simulation results discussed in this paper. Numerical convergence was checked by performing selected experiments with double resolution and half time step. For the wave-free simulation, we used a random low wavenumber initialization for the T and G modes, i.e., initial conditions were randomly prescribed for $k \leqslant 6$ in spectral space (and zero for higher wavenumbers) by setting $E_T = \text{Ro}^2$, $E_G = \text{Ro}^3$, Ro = 0.1 (as will be clear in Sec. III, we will examine the case $E_T = \text{Ro}^2$, $E_W = 1$ regime in great detail, making the present wave-free simulations a precursor for wave dominant regime simulations). Since oceanic observations and three-dimensional numerical simulations point out the dominance of geostrophic energy in the barotropic and the first baroclinic mode, with lesser and lesser energy in higher modes [23–26], we chose low energy for the high baroclinic G-mode relative to the barotropic mode.

Figures 2(a) and 2(b) show the barotropic vorticity and the baroclinic potential vorticity (PV) for this simulation, where we did not initialize waves. We observe the formation of large-scale coherent vortices in the barotropic flow while the baroclinic PV field behaves more like a passive tracer being stretched and deformed by the barotropic flow, resulting in the formation of small-scale vortices and filaments. Additionally, we find that the G-mode transfers energy to the T-mode over the duration of the simulation, as is shown in Fig. 2(c) (the green curve), while the T-mode gains energy (the
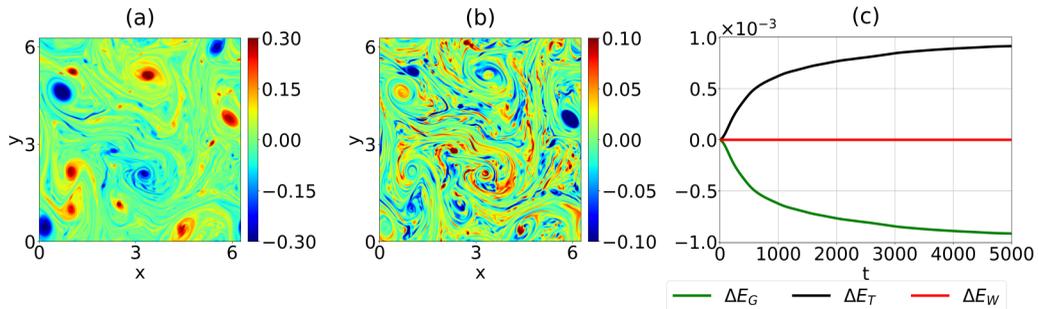
FIG. 2. (a) Barotropic vorticity and (b) baroclinic PV at $t = 5000$ based on a simulation of Eqs. (6) with initial conditions $E_T = \text{Ro}^2$, $E_G = \text{Ro}^3$, $E_W = 0$. (b) Energy change (from initial time) of T, G, and W modes.

black curve) conserving total energy of the system. Furthermore, although not initialized, some inertia-gravity waves are generated due to weakly nonlinear effects not captured to leading order in Eq. (12). However, these waves are extremely weak with insignificant energy content, as shown by the red curve in Fig. 2(c).

The phenomenology described above is as expected from QG dynamics based on Eq. (12) [22,27,28], and is shown schematically in Fig. 1 by different arrows. The inverse energy cascade that operates in the QG regime is known to transfer energy to low vertical wavenumbers (see, for example, freely evolving three-dimensional QG simulations investigated by [23–25]). In our two-vertical mode system, the high baroclinic G-mode undergoes a forward energy cascade and loses energy to the barotropic mode, while the barotropic mode gains energy and exhibits an inverse energy cascade. The small horizontal arrows in the T and G boxes in Fig. 1 symbolically represent the inverse and forward energy cascades of the barotropic and baroclinc flow, respectively, while the long blue arrow indicates energy transfer from the baroclinic to barotropic mode.

III. NEAR-INERTIAL WAVE EFFECTS ON GEOSTROPHIC TURBULENCE

As seen above, the barotropic flow organizes itself into large-scale coherent vortices in the absence of waves. In this section we will examine how such a phenomenology can be modified by NIWs. On exploring different parameter regimes of Eq. (6) by varying balance-to-wave energy ratio, we found weak interactions in cases where wave and balanced flow energies were comparable with the scaling $U_W \sim U_T$ or $E_W \sim E_T$. In contrast, significant energy exchanges and changes to the geostrophic turbulence phenomenology was observed in regimes with small balance-to-wave energy ratio. Specifically, consider the distinguished regime: $U_W \sim 1$ and $U_T \sim \text{Ro}$ (or $E_W \sim 1$ and $E_T \sim \text{Ro}^2$). This parameter regime, where waves are asymptotically stronger than the vortical field so that the $O(\text{Ro})$ nonlinear wave interaction terms such as Stokes drift and pseudomomentum are comparable in strength with the $O(\text{Ro})$ balanced flow, has been explored for surface waves [29–31], NIWs (XV, WY, RWY), and internal tides (TY). TY identifies this as the strong wave (SW) regime. Such high wave energy regimes are observed in the upper ocean when wind-forced NIWs are much stronger than pre-existing balanced flow. An example situation is discussed in D'Asaro et al. [32], where NIW velocity fields were observed to be an order of magnitude stronger than the balanced flow.

Consider a thought experiment ignoring the G-mode temporarily and treating the baroclinic mode (C) to consist of waves alone. In this case, the scaling $U_W \sim 1$ and $U_T \sim \text{Ro}$ imply that the barotropic-baroclinic interaction terms in Eqs. (6b) and (6c) scale as Ro^2, since Ro premultiplies the interaction terms. Consequently, weakly nonlinear modulation of waves by the balanced flow takes place on a timescale $1/\text{Ro}^2$. However, given that the waves' dispersion relationship is $\omega = \sqrt{1 + \text{Bu}\,k^2}$ with $\text{Bu} \ll 1$ for NIWs, slow modulation of the wave field due to dispersive effects take place on $1/\text{Bu}$ timescale. Significant interactions between NIWs and balanced flow takes place

when these two timescales match [see discussions in Thomas *et al.* [18]]. Consequently, we set $\text{Bu} \sim \text{Ro}^2$ in our numerical experiments. In numerical experiments we observed relatively high NIW-balanced flow energy exchanges for $\text{Bu} \leqslant \text{Ro}^2$ and weak interactions for $\text{Bu} \gg \text{Ro}^2$ (see the discussion related to Figs. 11 and 12 at the end of this section).

The same scaling described above—waves' dispersive timescale matching the wave-balance interaction timescale—was used in the asymptotic works of XV, WY, and RWY. However, there is a notable difference in the terminology we use in comparison to theirs. Recall that our investigation focuses on the weakly nonlinear dynamics of Eq. (6) in the regime $\text{Ro} \ll 1$. Within our model, examining the SW regime with $U_W \sim 1$ and $U_T \sim \text{Ro}$ (or $E_W \sim 1$ and $E_T \sim \text{Ro}^2$) implies that $\text{Ro} = U/fL$ is defined based on the wave velocity, i.e., $\text{Ro} = \text{Ro}_{\text{wave}} = U_W/fL$. (As pointed out below the nondimensionalization Eq. (4), the velocity scale U may be thought of as the largest velocity value prescribed initially. Since SW regime consists of high-energy waves and weak balanced flow, U would be the scale for wave velocity, which appears in the definition of Ro.) Concomitantly, since $U_T/U_W \sim \text{Ro}$, the Rossby number based on velocity scale of the barotropic flow would be $\text{Ro}_{\text{balanced}} = U_T/fL = \text{Ro}^2$. Therefore by setting $\text{Bu} \sim \text{Ro}^2$, we are basically demanding that the Burger number is of the same order as the Rossby number defined based on the balanced velocity field, i.e., $\text{Bu} \sim \text{Ro}_{\text{balanced}}$. This exact scaling, i.e., $\text{Bu} \sim \text{Ro}_{\text{balanced}}$, was used in the asymptotic works of XV, WY, and RWY, with the key difference that they define Rossby number based on balanced velocity.

Based on the above discussions, we will now examine results of a specific simulation that used parameters: $\text{Bu} = \text{Ro}^2$, $E_W = 1$, $E_T = \text{Ro}^2$, and $E_G = 0$ with $\text{Ro} = 0.1$ in great detail, and then briefly discuss results in neighboring parameter regimes at the end of this section. We chose spatially homogeneous initial data for the wave field as $u_W = c$, $v_W = p_W = 0$, where the constant c was fixed by setting $E_W = 1$. The barotropic flow was initialized with $E_T = \text{Ro}^2$ using uncorrelated random numbers at low wavenumbers ($k \leqslant 6$). On experimenting with different E_G initial values such that $E_G \ll E_T$ at $t = 0$, we found almost no changes in turbulence phenomenology discussed below, indicating that the magnitude of E_G has a relatively weak influence on the turbulent dynamics of the reduced model we examine. Additionally, on setting $E_G = 0$ at $t = 0$, we found that the G-mode extracts some energy from other modes, resulting in small but nonzero value for E_G at $t > 0$. We therefore set $E_G = 0$ in this specific experiment we discuss in detail, allowing the G-mode to evolve to an energy level based on its interaction with other modes, rather than prescribe it initially.

For the initial value problem described above, Fig. 3 shows the spatial structure, energy spectra, and frequency spectra of the fields. As seen in Figs. 3(a)–3(d), the barotropic flow although shows a tendency for vortex mergers early on, the flow develops a cascade to small scales, resulting in the formation of small-scale vortices. The baroclinic balanced flow, although not initialized, is generated by the interaction between waves and the barotropic flow. The magnitude of the baroclinic balanced flow remains small throughout and was seen to have similar spatial structures as those of the barotropic balanced flow shown in the first row of Fig. 3 (figures omitted). The wave field, although homogeneous initially, generates small-scale features [see Figs. 3(e)–3(h)]. Figures 3(i)–3(l) shows the energy spectra of W, T, and G modes. Observe the spikes that appear in the waves' energy spectra (the red curve) in Figs. 3(i) and 3(j). These spikes correspond to higher harmonics, $\omega = 2, 3, 4$, etc. Eventually, these higher harmonic waves start dominating over the balanced flow energy at these scales: notice the wave energy spectrum climbing over the balanced flow spectrum in Fig. 3(k). This process culminates in a state where a significant range of the waves' spectrum dominates over the T-mode's spectrum, as seen in Fig. 3(l). Figures 3(m)–3(p) show the frequency spectrum of u_W at different times. Each frequency spectrum shown was obtained by ensemble averaging the frequency spectrum of 10 arbitrary grid points. The waves' frequency spectra clearly show a broadening with the generation of higher harmonics from the initial spatially homogeneous inertial oscillations. Notice that the spectrum at early times [Fig. 3(m)] is quite narrow with a sharp decay away from the inertial frequency $\omega = 1$. However, the generation of smaller scales in the wave field is accompanied by the generation of higher wave harmonics, resulting in a broadband wave frequency spectrum, as seen in Fig. 3(p).
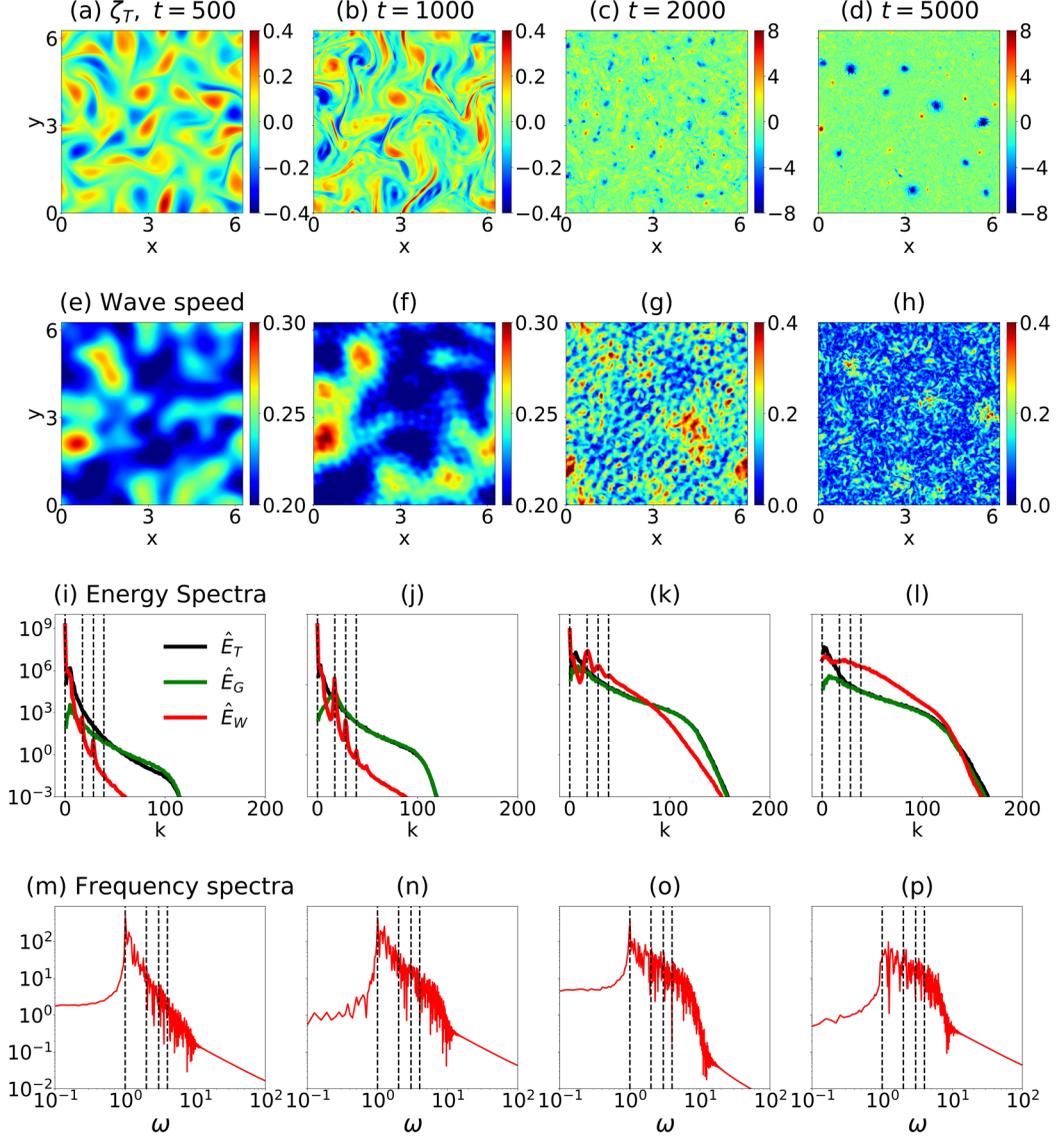
FIG. 3. Results of a simulation with $\mathrm{Bu} = \mathrm{Ro}^2$ and $\mathrm{Ro} = 0.1$ with initial conditions: $E_T = \mathrm{Ro}^2$, $E_G = 0$, and $E_W = 1$. (a)–(d) ζ_T, (e)–(h) wave speed, $\sqrt{u_W^2 + v_W^2}$ (i)–(l) total energy spectra of T, W, and G, and (m)–(p) frequency spectra of u_W. The four columns above correspond to four different times indicated above the first row. The dashed vertical lines in frequency spectra correspond to frequencies: $\omega = 1, 2, 3,$ and 4. The wavenumbers corresponding to these frequencies were obtained based on the dispersion relationship $\omega(k) = \sqrt{1 + \mathrm{Bu}\, k^2}$ and are marked by dashed vertical lines in the energy spectra.

Trapping of NIWs in anticyclonic vortical regions is a feature often seen in oceanic observations and large-scale ocean model simulations [see, for example, Lee and Niiler [33] and Elipot *et al.* [34]]. To check this feature in our idealized model, we computed the quantity R defined as

$$R = \frac{\langle \zeta_T E_W^{KE} \rangle}{\sqrt{\langle \zeta_T^2 \rangle \langle E_W^{KE\,2} \rangle}}, \tag{13}$$
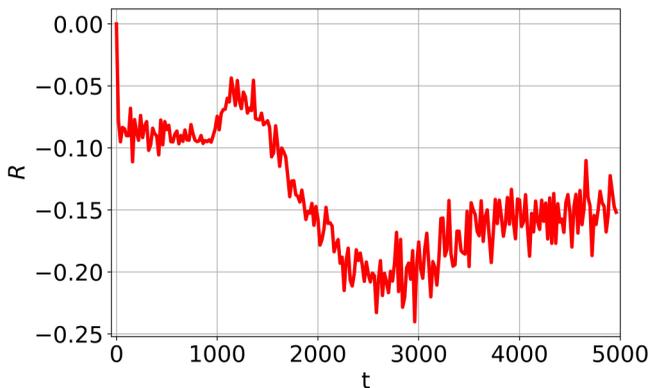
FIG. 4. Plotted above is the time series of the variable R defined in Eq. (13). Observe that R is negative throughout, indicating that waves are positively correlated with anticyclonic regions in ζ_T, i.e., regions where $\zeta_T < 0$.

where $E_W^{KE} = 1/2(u_W^2 + v_W^2)$ is the wave kinetic energy (WKE) and angle brackets denote spatial averaging over the domain. Figure 4 shows a time series of R for the experiment detailed in Fig. 3. Observe that R is negative throughout, indicating the positive correlation between waves and negative ζ_T regions (or anticyclones). An explanation for trapping of NIWs in anticyclonic vortical regions based on conservation laws of NIW amplitude equations in different parameter regimes can be developed when the barotropic flow is steady in time [see discussions in Danioux *et al.* [17] and Thomas *et al.* [18]]. However, no similar straightforward explanation is available when the barotropic flow evolves in time, as in our case, although trapping of waves in anticyclones is reported in such cases as well (see discussions in RWY). Furthermore, we infer from Fig. 4 that R is negative at all times, both at short times when wave and balanced fields are concentrated at large scales, and at long times when wave and balanced fields consists of fine scale features.

In Fig. 5 we quantify the transition of the wave field from large-scale NIWs to small-scale high-frequency inertia-gravity waves. Pure inertial oscillations, which was excited by our homogeneous initial conditions, have zero wave potential energy (WPE) and nonzero wave kinetic energy. The ratio of WPE to WKE plotted in Fig. 5(a) (the red curve) therefore starts at zero, although the formation of small-scale features in the wave field seen in Fig. 3 is accompanied by an increase in this ratio. The accelerated increase in the WPE:WKE ratio starts close to $t = 1000$, and continues
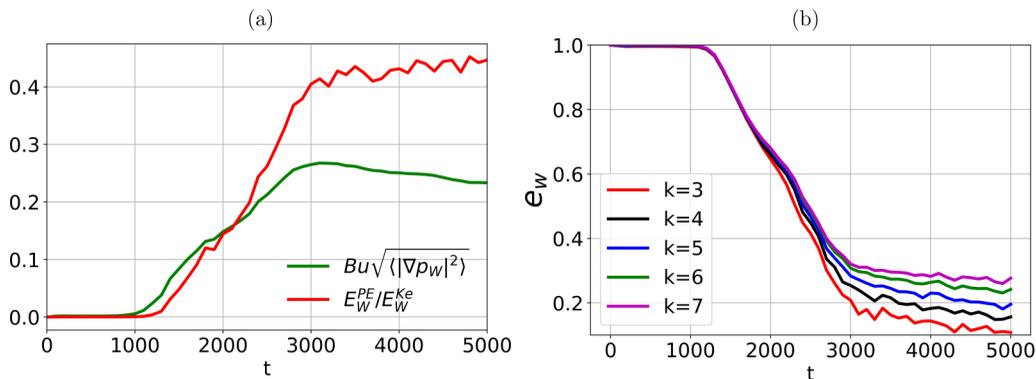
FIG. 5. (a) WPE:WKE ratio and the root-mean-square pressure gradient term. (b) $e_W(k, t)$ showing the fraction of the total wave energy contained in wavenumbers lower than k; see Eq. (14).

until roughly around $t = 3000$, after which it asymptotes. Consequently, the wave field may be identified as near-inertial for $t < 1000$, undergoing a transition to high-frequency waves from $t = 1000$ to 3000, and as high-frequency waves for $t > 3000$. The curve showing root-mean-square value of the waves' pressure gradient term: $\mathrm{Bu}\sqrt{\langle (\nabla p_W)^2 \rangle}$ in Fig. 5(a) adds to the previous description. The pressure gradient term is asymptotically weak for NIWs, but becomes $O(1)$ as high-frequency waves form. The transition from NIWs to high-frequency waves is further clarified by Fig. 5(b), which shows the fractional wave energy contained in low wavenumbers calculated as

$$e_W(k, t) = \left[\sum_{s=0}^{s=k} \hat{E}_W(s, t) \right] \Big/ \left[\sum_{s=0}^{s=k_{\max}} \hat{E}_W(s, t) \right], \tag{14}$$

where $\hat{E}_W(s, t)$ denotes the total wave energy associated with wavenumber s. Since the waves' dispersion relationship is $\omega(k) = \sqrt{1 + \mathrm{Bu}\, k^2}$, the frequencies of the wavenumbers shown in Fig. 5(b) are $\omega(3) = 1.04$, $\omega(4) = 1.08$, $\omega(5) = 1.12$, $\omega(6) = 1.17$, and $\omega(7) = 1.22$ (using $\mathrm{Bu} = \mathrm{Ro}^2 = 0.01$). We may choose $k = 6$ as the cutoff wavenumber and identify higher wavenumbers to be outside the near-inertial frequency range, since wavenumbers $k > 6$ have frequency exceeding the inertial frequency by more than 20%. Based on $k = 6$ as the cutoff wavenumber, we find that by $t = 5000$ only 25% of the wave energy can be identified to be near-inertial, with the rest 75% constituting high-frequency waves. If we chose a lower wavenumber as the cutoff wavenumber, lesser energy would be associated with near-inertial waves by $t = 5000$. Irrespective of this cutoff wavenumber, Fig. 5(b) shows that the transition to high-frequency waves begin roughly at $t = 1000$ and starts asymptoting around $t = 3000$.

Our examination of Fig. 5 helps us identify three different phases across which the dynamics span. The first phase, roughly span up to $t = 1000$, and the wave field is near-inertial during this period. The first and second column of Fig. 3 belongs to the first phase, characterized by the near-inertial wave field acquiring spatial scales of the barotropic flow, and the barotropic flow beginning to exhibit vortex mergers. Additionally, the generation of higher wave harmonics begins in this phase [marked by the spikes in the wave energy spectra shown in Figs. 3(i) and 3(j)], although these higher harmonics are energetically weak in this phase. The second phase spans from $t = 1000$ to 3000 and is the transition phase where the wave field changes from near-inertial to predominantly high-frequency waves. The third column of Fig. 3 belongs to this phase, where both the wave and the barotropic mode exhibits a transition from large to small scales, along with the formation of high-frequency wave components which start to dominate over the barotropic mode's energy as can be seen in the energy spectra in Fig. 3(k) (recall the red curve overtaking the black curve there). The final phase goes from $t = 3000$ onward, consisting of a broadband high-frequency wave field and a barotropic flow field dominated by small-scale structures. As seen in the energy spectrum in Fig. 3(l), the waves dominate over the balanced flow across a range of scales in this final phase.

We next examine energy exchange between waves and the balanced flow during these different phases. Figure 6 shows the time series of the energy changes in T, W, and G modes, and additionally the kinetic and potential energy change of waves. The three different phases discussed before can be identified in Fig. 6(b). The first phase, roughly extending up to $t = 1000$, consists of relatively low-energy transfers. For better visibility, part of this phase is shown in detail in Fig. 6(a). During all three phases, we observe that wave potential energy (red curve with triangle markers) increases, although wave kinetic energy (red curve with circular markers) decreases by a larger magnitude, resulting in net drop in wave total energy (red curve with no markers). We also observe that the G-mode's energy (green curve) changes only by a negligible amount. Consequently, apart form the energy lost to dissipation, the drop in waves' total energy is compensated by an increase in the barotropic modes energy (black curve). Aside from the specific details we discuss below, the following observation summarizes the net energy exchange between waves and the balanced flow throughout the evolution of the system: total wave energy decreases and the barotropic energy increases, while negligible energy change is associated with the baroclinic balanced flow.
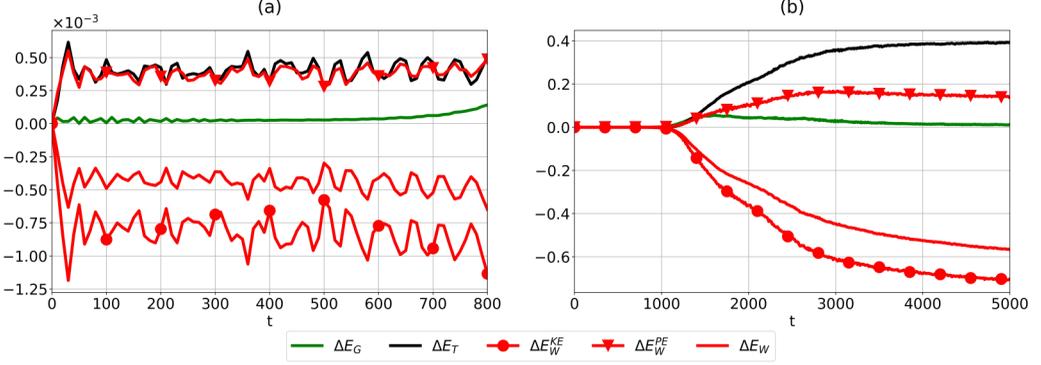
FIG. 6. Change in energy of T, W, and G modes, and WPE and WKE. Panel (a) shows a short duration of phase 1 while panel (b) shows the entire duration of the dynamics.

To examine the wave-balance triads responsible for the above described energy exchanges, we apply the linear wave-balance decomposition to the governing equations. This gives us the energy evolution equations of the three modes (similar analysis using three-dimensional models can be found in Waite [12] and Deusebio *et al.* [10]). The energy equations of the T, W, and G modes are

$$\frac{\partial \hat{E}_T(k,t)}{\partial t} = \hat{T}_{TTT}(k,t) + \hat{T}_{TGG}(k,t) + \hat{T}_{TGW}(k,t) + \hat{T}_{TWW}(k,t) - \hat{D}_T(k,t), \tag{15a}$$

$$\frac{\partial \hat{E}_W(k,t)}{\partial t} = \hat{T}_{WTG}(k,t) + \hat{T}_{WTW}(k,t) - \hat{D}_W(k,t), \tag{15b}$$

$$\frac{\partial \hat{E}_G(k,t)}{\partial t} = \hat{T}_{GTG}(k,t) + \hat{T}_{GTW}(k,t) - \hat{D}_G(k,t). \tag{15c}$$

In the above equations, $\hat{E}_T(k,t) = |\hat{v}_T(k,t)|^2$ is the T-mode's energy, $\hat{E}_W(k,t) = |\hat{v}_W(k,t)|^2 + |\hat{p}_W(k,t)|^2$ is the total wave energy (sum of kinetic and potential energies), and $\hat{E}_G(k,t) = |\hat{v}_G(k,t)|^2 + |\hat{p}_G(k,t)|^2$ is the G-modes total energy at a specific wavenumber k. The $\hat{T}(k,t)$ terms on the right-hand side capture different triadic interactions between T, W, and G modes. Finally, the $\hat{D}(k,t)$ terms above refer to the hyperdissipation acting at the wavenumber k.

We sum the terms in Eq. (15) from $k = k_{\max}$ to $k = 0$ to get the total energy change associated with each specific term. We further time-integrate each term thus obtained from 0 to t to get net energy change and associated interaction terms as

$$\Delta E_T(t) = E_T(t) - E_T(0) = E_{TGG}(t) + E_{TGW}(t) + E_{TWW}(t) - D_T(t), \tag{16a}$$

$$\Delta E_W(t) = E_W(t) - E_W(0) = E_{WTG}(t) + E_{WTW}(t) - D_W(t), \tag{16b}$$

$$\Delta E_G(t) = E_G(t) - E_G(0) = E_{GTG}(t) + E_{GTW}(t) - D_G(t). \tag{16c}$$

The term E_{TTT} is zero (since barotropic triadic interactions cannot change net energy of the barotropic mode) and is therefore not included in Eq. (16a). The triadic terms in Eqs. (16) conserve energy with respect to the specific set of modes considered, due to which we have the auxiliary relationships:

$$E_{TWW}(t) + E_{WTW}(t) = 0, \tag{17a}$$

$$E_{TGG}(t) + E_{GTG}(t) = 0, \tag{17b}$$

$$E_{TGW}(t) + E_{WTG}(t) + E_{GTW}(t) = 0. \tag{17c}$$

Equation (17a) states the condition that the total energy exchange between waves and the barotropic mode must be conserved under nonlinear interactions, while Eq. (17b) is a similar condition for energy exchange between G and T modes. Finally, Eq. (17c) expresses the constraint that total energy exchange due to mixed barotropic-baroclinic balanced-wave modes must be conserved.

Figure 7 shows the time evolution of the terms in Eq. (16). For convenience in interpreting results, we present the barotropic energy budget in Figs. 7(a) and 7(b), wave energy budget in Figs. 7(c) and 7(d), and the baroclinic balanced flow's energy budget in Figs. 7(e) and 7(f). As in Fig. 6, we split Fig. 7 to show a shorter duration on the left and the entire duration on the right. In the first phase, Fig. 7(a) shows that the barotropic energy increases (black curve) due to direct transfer by NIWs via the term E_{TWW} (see the blue curve), other triadic interaction terms being relatively weak. On checking the waves' energy budget given in Fig. 7(c), we find that NIWs lose energy (continuous red curve) exclusively due to transfer to the T-mode via the triad E_{WTW} (blue curve), the triad E_{WTG} being insignificant (note that the curves E_{WTG} and D_W lie on top of each other and are negligible in magnitude). Finally, observe in Fig. 7(e) that the G-mode's energy, although initially zero, increases (see the green curve), the triadic term E_{GTW} (see the brown curve) acting as the primary source. We also note that dissipation is almost entirely negligible in the first phase: observe that the dashed curves in Figs. 7(a), 7(c), and 7(e) representing energy dissipation of T, W, and G-mode are insignificant. The first phase is therefore characterized by NIWs directly feeding the barotropic balanced flow as per Eq. (17a).

The second phase extending roughly from $t = 1000$ to 3000 is characterized by accelerated energy transfers between different modes. The formation of energetic high-frequency and smaller scale wave field features (seen in the third column of Fig. 3) goes hand-in-hand with rapid drop in the wave energy and corresponding increase in the barotropic mode's energy, as seen in the black and red curves in Figs. 7(b) and 7(d), respectively. On examining the detailed energy transfer terms in Fig. 7(b), we find that the barotropic mode receives energy via direct transfer from waves via the term E_{TWW} (blue curve) and the baroclinic balanced flow via the term E_{TGG} (orange curve) while the mixed triadic term E_{TGW} (brown curve) acts as its energy sink. The effects of E_{TGG} and E_{TGW} are almost equal and opposite, resulting in T-mode gaining energy as if direct transfer by the E_{TWW} term was its sole source. On examining the waves' energy budget in Fig. 7(d), we see that the wave energy decreases due to the direct transfer to the barotropic mode via the E_{WTW} term (blue curve). Additionally, we observe that E_{WTG} (brown curve) is small but negative, forming a sink for wave energy. Therefore, although phase 2 is characterized by significantly more energy changes than phase 1, the net energy transfer directions are similar in these two phases: waves lose energy and the barotropic flow gains energy, while the G-mode has little energy. Examining the G-mode's energy budget in Fig. 7(f) reveals the reason for G-mode's little energy content. Observe that although the G-mode is fed directly by the mixed triadic E_{GTW} term (see brown curve), almost comparable amount of energy is transferred by the G-mode directly to the T-mode via the E_{GTG} term (orange curve) resulting in little increase in the energy of the G-mode. A distinct feature of the second phase, in addition to the formation of small scales in wave and balanced flow and the rapid energy exchanges described above, is that dissipation of the flow begins here, as seen by examining the dashed curves in Figs. 7(b), 7(d), and 7(f). The dissipation curves start to become nonzero roughly around $t = 2000$, steadily dropping thereafter. This is an indication that the small scales formed in phase 2, seen in Figs. 3(c) and 3(g) have started reaching dissipative scales.

The final phase, roughly extending from $t = 3000$ to 5000 is characterized by similar energy transfer directions as in phase 2, although the magnitudes of energy change decreases. The barotropic energy is seen to reach a saturated state [black curve in Fig. 7(b)] although waves continue to lose energy [red curve in Fig. 7(d)], with wave dissipation being significant in this phase. The G-mode behaves as in phase 2: the energy gain from E_{GTW} almost equals energy loss via E_{GTG} resulting in negligible net energy gain for the G-mode [green curve in Fig. 7(f)].
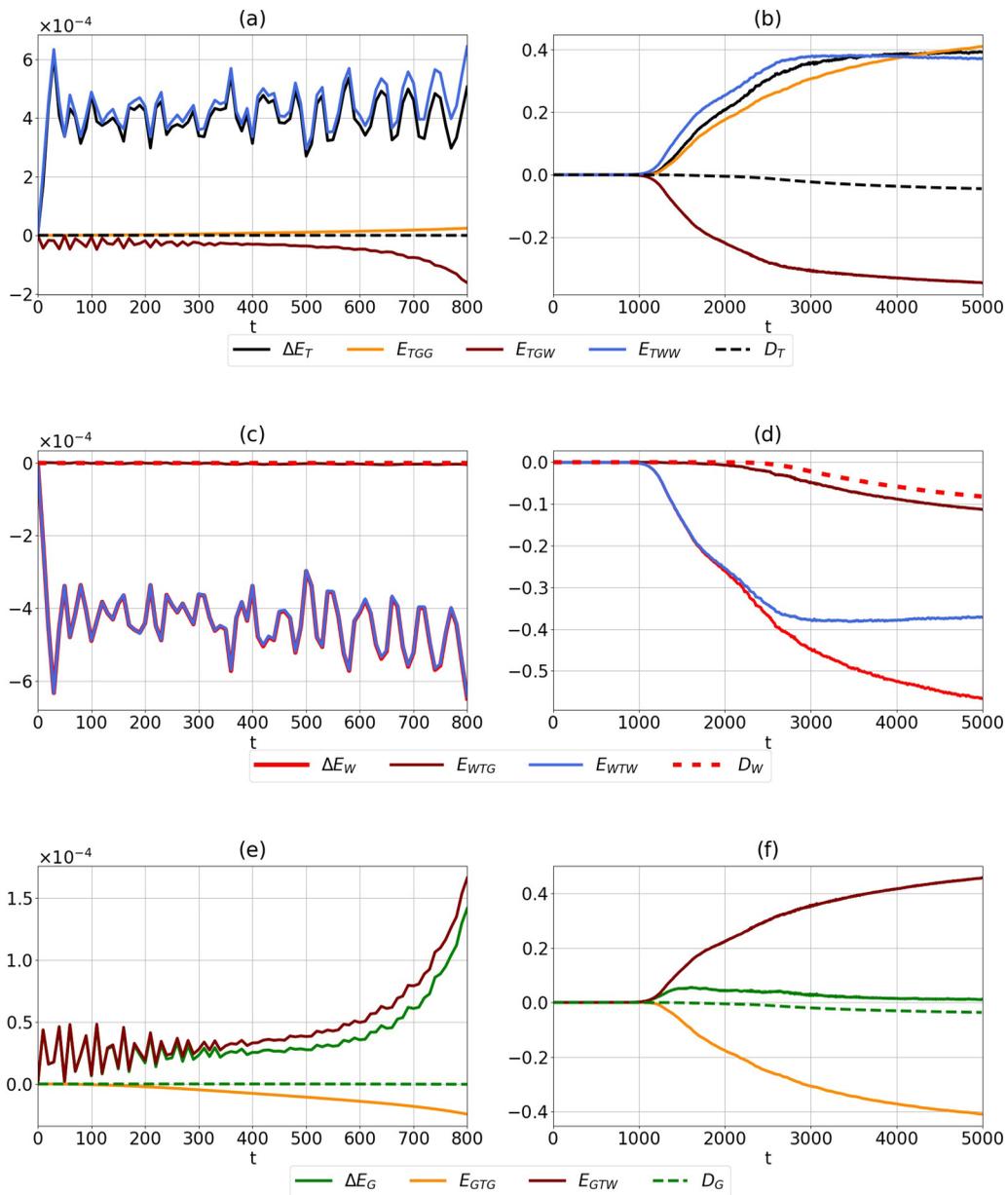
FIG. 7. Time series of the energy exchange terms given in Eq. (16). Panels (a) and (b) show the barotropic mode's budget based on Eq. (16a); panels (c) and (d) show the wave's budget based on Eq. (16b); and panels (e) and (f) shows the baroclinic balanced flow's budget based on Eq. (16c). Note that in panel (c) above, the time series of E_{WTW} and ΔE_W overlap, while E_{WTG} and D_W are negligible in magnitude and lie on top of each other.

To complement above examination of the net energy exchanges between modes, we will now examine the spectral fluxes. This will clarify the energy flow pathways across spatial scales in each mode. We sum Eq. (15) from the maximum wavenumber $k_{\max}$ to k to obtain the energy flux

equations of T, W, and G modes as

$$\frac{\partial E_T^\Pi(k,t)}{\partial t} = \underbrace{\Pi_{TTT}(k,t) + \Pi_{TGG}(k,t) + \Pi_{TGW}(k,t) + \Pi_{TWW}(k,t)}_{\Pi_T} - D_T^\Pi(k,t), \quad (18a)$$

$$\frac{\partial E_W^\Pi(k,t)}{\partial t} = \underbrace{\Pi_{WTG}(k,t) + \Pi_{WTW}(k,t)}_{\Pi_W} - D_W^\Pi(k,t), \quad (18b)$$

$$\frac{\partial E_G^\Pi(k,t)}{\partial t} = \underbrace{\Pi_{GTG}(k,t) + \Pi_{GTW}(k,t)}_{\Pi_G} - D_G^\Pi(k,t), \quad (18c)$$

Eq. (18a) is the equation for the rate of change of the barotropic energy $E_T^\Pi(k,t)$ contained in the spectral band $[k, k_{\max}]$, i.e., $E_T^\Pi(k,t) = \sum_{s=k_{\max}}^{k} \hat{E}_T(s,t)$. The barotropic flux Π_T and dissipation D_T^Π constitute the right hand side of Eq. (18a). Notice that the total barotropic flux Π_T is the sum of four different triadic contributions, i.e., $\Pi_T = \Pi_{TTT} + \Pi_{TGG} + \Pi_{TGW} + \Pi_{TWW}$. Similarly, Eqs. (18b) and (18c) gives the spectral energy flux equations of W and G-modes with their respective fluxes Π_W and Π_G being decomposed in to separate triadic contributions such that $\Pi_W = \Pi_{WTG} + \Pi_{WTW}$ and $\Pi_G = \Pi_{GTG} + \Pi_{GTW}$. The triadic fluxes given in Eqs. (18) are plotted at $t = 2000$ in Fig. 8, with separate plots corresponding to large scales, $k \leqslant 15$, on the left and smaller scales, $k > 15$, on the right.

Observe in Figs. 8(a) and 8(b) that the total barotropic energy flux, Π_T, is positive at both large and small scales, indicating a forward cascade of T-mode's energy. At large scales ($k \leqslant 15$), both Π_{TWW} and Π_{TGG} are positive and comparable, whose sum over powers the negative flux due to Π_{TTT} and Π_{TGW}. In contrast, at smaller scales ($k > 15$), Π_{TGG} is weak and the positive value of Π_{TWW} alone over comes the negative flux due to Π_{TTT} and Π_{TGW}. Consequently, we conclude that the waves assist in the forward energy cascade of the barotropic flow. We also observe that the total wave energy flux Π_W is positive in Figs. 8(c) and 8(d), indicating a forward wave energy cascade. At large scales, $k \leqslant 15$, the wave flux is dominated by Π_{WTG}, which exceeds Π_{WTW}, both being positive. Π_{WTG} is seen to be positive at smaller scales as well, though it is much smaller in magnitude compared to Π_{WTW}. The balanced flow—both barotropic and baroclinic—therefore assists in the forward cascade of wave energy. Finally, the G-mode's energy fluxes shown in Figs. 8(e) and 8(f) point out that except for the first few wavenumbers, the total G-flux Π_G is positive with dominant contribution from the Π_{GTG} flux—indicating a forward cascade of G-mode's energy.

Our examination of spectral fluxes above points out that all three modes—T, W, and G—undergo a forward energy cascade, which concur with the physical fields shown in Fig. 3. The wave field is assisted by the barotropic and baroclinic balanced flow in its forward cascade, resulting in a high-frequency wave field with small scales. Additionally, the wave field facilitates the forward cascade of the balanced flow energy, especially the barotropic flow, resulting in the formation of small-scale features in the barotropic flow. The forward cascade of wave and balanced flow fields therefore goes hand in hand with the energy transfer from waves to the barotropic balanced flow. In the interest of space we discussed spectral fluxes only at a certain time (shown in Fig. 8), although similar qualitative phenomenology was observed at different times we checked. At earlier times the fluxes were primarily concentrated at large scales with smaller values at high wavenumbers, while at late times we found that the magnitudes of the fluxes were higher than those seen in Fig. 8 at high wavenumbers.

Given above description of the energy exchange between waves and balanced flow, we recall that all of the analysis so far relies on the linear wave-balance decomposition, i.e., the barotropic flow is in geostrophic balance, while the baroclinic flow is orthogonally decomposed into inertia-gravity waves and a geostrophically balanced flow. To examine the wave field in more detail, we checked the frequency spectra of individual wavenumbers of the wave field at different times and an example is given in Fig. 9, which shows the frequency spectra of the wave field corresponding to three different
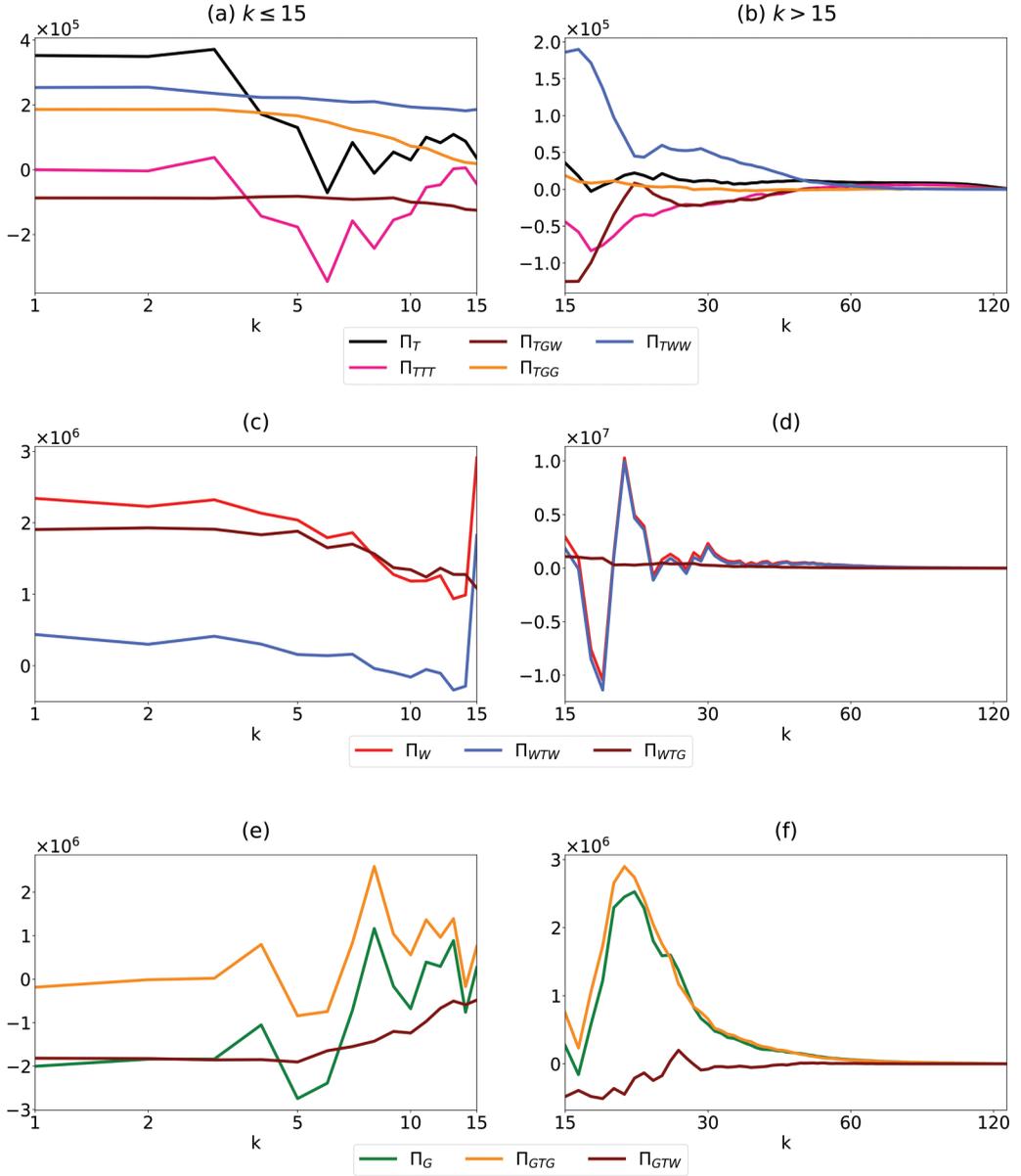
FIG. 8. Spectral fluxes computed at $t = 2000$ based on Eq. (18). The fluxes were time-averaged over a window $\Delta t = 25$ to remove high-frequency fluctuations.

wavenumbers. Observe that the red colored frequency spectra in Fig. 9, obtained from numerical simulations, peaks around the linear wave frequency (obtained from the dispersion relationship at those wavenumbers and is shown by dashed vertical lines) and rapidly decays away from it. The numerical and linear waves' frequency predictions agree quite well, except for high wavenumbers with less energy (notice that the y-axis maxima of Fig. 9 drops with increasing k). This behavior, of high wavenumbers with low-energy levels showing slight departures from linear wave frequencies, is expected in wave-turbulence interaction experiments since the wave-balance decomposition based on the linear equations would break down at smaller scales, where the distinction between linear
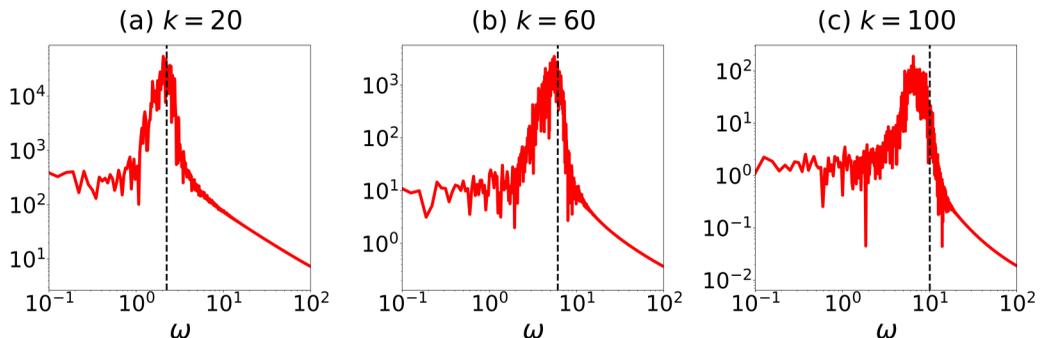
FIG. 9. Frequency spectra of three wavenumbers. The dashed vertical lines on each plot indicate the linear wave frequency corresponding to that specific wavenumber based on the dispersion relationship: $\omega(k) = \sqrt{1 + \mathrm{Bu}\, k^2}$.

wave and turbulent dynamics is lost (see Kafiabad and Bartello [35] and Deusebio *et al.* [10] for similar phenomenology in three dimensions). Based on our waves' frequency spectra analysis, we conclude that the wave field interacting and exchanging energy with the balanced flow is predominantly linear.

We next examine the frequency spectra of the barotropic flow, which based on our examination of Figs. 6 and 7 gains almost the entire energy lost by the waves, apart from dissipation. Since the wave energy is $O(1)$ and balanced energy is $O(\mathrm{Ro}^2)$ in this regime, nonlinear wave interactions would project on the barotropic flow, resulting in high-frequency fluctuations in the barotropic flow. This is confirmed in Fig. 10(a), where the black curve shows the frequency spectrum of u_T obtained by ensemble averaging the frequency spectrum of 10 arbitrary grid points. Notice that high-frequency fluctuations are present in this frequency spectrum, showing the effect of wave-interactions. To extract a slow-evolving barotropic flow from the total barotropic flow, we performed a running time average of the barotropic vorticity:

$$\overline{\zeta_T}(x, y, t) = \frac{1}{\Delta t} \int_{t-\Delta t/2}^{t+\Delta t/2} \zeta_T(x, y, \tau)d\tau, \qquad (19)$$

which was used to compute the slow-evolving barotropic fields and thereby the slow-barotropic energy. We used $\Delta t = 25$ as our averaging window width. The red curve in Fig. 10(a) shows the
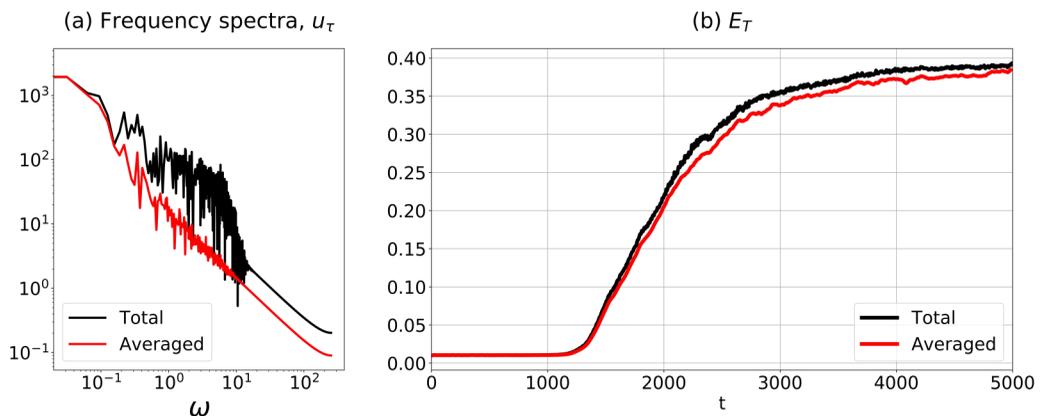
FIG. 10. (a) Frequency spectrum of u_T before (black) and after (red) the running time averaging based on Eq. (19) was performed. (b) Evolution of the slow (red) and unaveraged (black) barotropic flow energy.
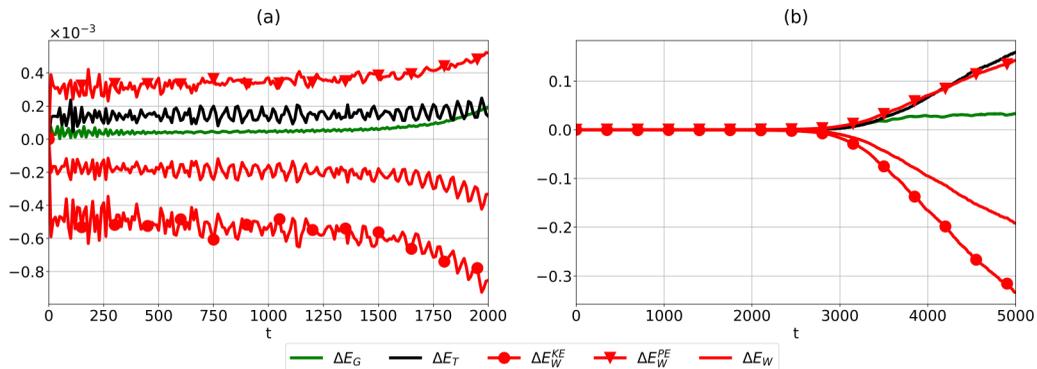
FIG. 11. $Bu = 2Ro^2$ with initial conditions: $E_T = Ro^2$, $E_G = 0$, and homogeneous wave field with $E_W = 1$.

time averaged frequency spectrum, from which it is clear that the time averaging operation reduces high-frequency fluctuations. Figure 10(b) shows the evolution of the total barotropic flow energy and the slow-barotropic flow energy. We find that the slow energy agrees with the total energy quite well, the difference being less than 4%. We therefore conclude that the energy gain of the barotropic flow is primarily associated with the slow-component, with fast fluctuations carrying negligible energy.

Having examined the case $Bu = Ro^2$ with initial conditions: $E_T = Ro^2$, $E_G = 0$, and homogeneous initial wave field with $E_W = 1$, we will now briefly discuss how the above results would differ on changing parameters. Although the simulation described before used a spatially homogeneous initial NIW field, we found similar phenomenology on initializing the simulations with a spatially inhomogeneous NIW field. Similarly, the previously discussed dynamics used $E_G = 0$ at $t = 0$, although the G-mode was seen to extract some energy as the flow evolved. The initial value of E_G was not seen to influence the phenomenology discussed in detail earlier. We found similar qualitative behavior on initializing the system with nonzero E_G values, such as $E_G = Ro^3$ while $E_T = Ro^2$. We conclude this section by discussing two different cases obtained by changing Bu. To examine the effect of the Burger number, we simulated two cases with $Bu = 2Ro^2$ and $Bu = Ro^2/2$ while $Ro = 0.1$, the results being shown in Figs. 11 and 12. Observe that a higher Bu ($=2Ro^2$) delays the transition from phase 1 almost until $t = 3000$ while a lower Bu ($=Ro^2/2$) accelerates the transition, which takes place around $t = 500$. We therefore conclude that the phenomenology described in detail earlier in this section would take place much more rapidly for high baroclinic modes and slower for low baroclinic modes.
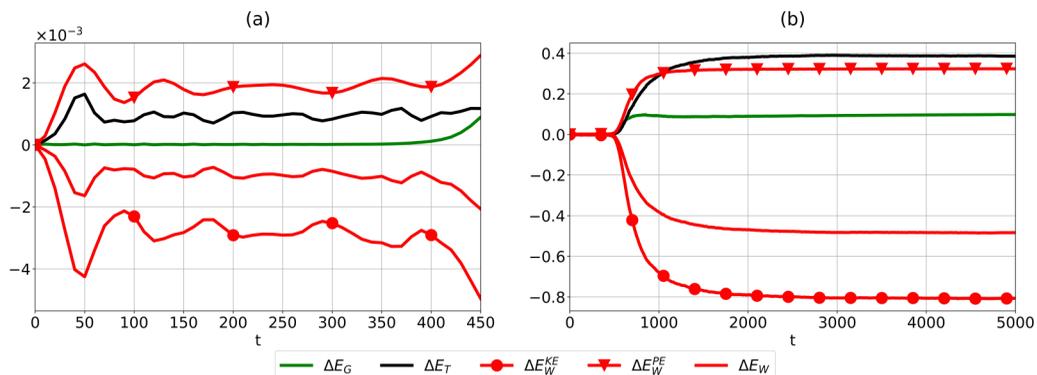
FIG. 12. $Bu = Ro^2/2$ with initial conditions: $E_T = Ro^2$, $E_G = 0$, and homogeneous wave field with $E_W = 1$.
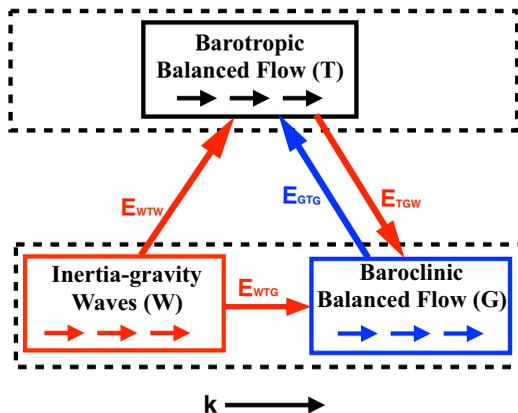
FIG. 13. Schematic showing energy flow pathways between the three modes based on our simulations. The barotropic flow receives energy from waves via the E_{WTW} term. Although the baroclinic balanced flow gains energy from both waves and the barotropic mode by $E_{GTG} = E_{WTG} + E_{TGW}$, the magnitude of this energy gain is comparable with the amount of energy the baroclinic balanced mode directly transfers to the barotropic mode via the E_{GTG} term. As a result, the baroclinic balanced mode's energy remains relatively small at all times. Importantly, all three modes exhibit a forward energy cascade, resulting in the generation of small-scale features in the balanced and wave fields. The small horizontal arrows pointing right indicates this, wavenumber k increasing from left to right. Concomitant with the generation of small-scale features, the waves' forward energy cascade transforms the wave field from NIWs at early times to a high-frequency inertia-gravity wave field at later times.

Based on our analysis so far, the energy flow pathways within our reduced model is summarized in Fig. 13, with the arrows between the boxes denoting the energy transfer between modes while arrows within each box denotes energy flow within each mode. Overall, the barotropic flow gains energy from waves (E_{WTW}) and the baroclinic balanced flow (E_{GTG}). The baroclinic balanced flow's energy remains significantly weak at all times, since the energy it gains from waves and the barotropic flow ($E_{GTW} = E_{WTG} + E_{TGW}$) is close to the amount it loses to the barotropic flow (E_{GTG}). Consequently, the net energy exchange between the three modes may therefore be summarized as waves losing energy and the barotropic flow gaining energy.

We conclude this section by comparing our findings with that of TY, where low mode internal tide-balanced flow interactions were examined. To capture the dynamics of internal tides, TY used the first baroclinic mode resulting in Bu $\sim O(1)$. Additionally, the usage of the first baroclinic mode meant that the G-mode in that study contained energy comparable to the T-mode. In contrast, we used a high baroclinic mode with Bu $\ll 1$, resulting in a G-mode containing significantly low energy compared to the T-mode. The G-mode was seen to be energetically weak throughout the duration of our experiments. Another distinguished feature of this study is the forward energy cascade of the modes. No forward energy cascade of the modes were observed in TY, since all the energy exchanges and turbulence phenomenology was observed to take place at large scales (see Fig. 8 there). In contrast, NIW-balanced flow interactions in Bu $\ll 1$ regime exhibits a forward energy cascade of both wave and balanced fields, resulting in small-scale features. This suggests a transition of the turbulent energy flow pathways as one decreases Bu from $O(1)$ values to asymptotically small values, this transition being similar to that exhibited in many other physical systems as detailed in Alexakis and Biferale [36].

IV. SUMMARY AND DISCUSSION

NIWs, generated by atmospheric winds and storms, is an energetically dominant wave field in the upper ocean and their weakly dispersive nature gives rise to the possibility of energy exchange with pre-existing mesoscale balanced flow. An improved understanding of various wave-balanced flow

energy exchanges is crucial to uncover detailed oceanic energy flow pathways. Such investigations, i.e., energetic interactions between NIWs and balanced flow, have been undertaken in both low and high Rossby number regimes. Notably, multiple NIW-balanced flow investigations in the low Rossby number regime have taken advantage of approximate asymptotic coupled NIW-balanced flow interaction models (XV, WY, and RWY). Our goal in this work was to examine energy exchanges between NIWs and balanced flow in the Ro ≪ 1 regime using an idealized model without relying on asymptotics. Towards this goal, we derived a reduced nonasymptotic model by projecting the hydrostatic Boussinesq equations onto the barotropic and a single high baroclinic mode.

We begin with the obvious: although our model was nonasymptotic and consists of richer dynamics than asymptotic models mentioned above, the two-vertical-mode equations definitely loses some of the crucial features of the three-dimensional Boussinesq equations. Therefore the reader is once again reminded that the results we discuss are strictly within our restricted two-dimensional system. The two-vertical mode model consists of three components: barotropic balanced flow (T), baroclinic balanced flow (G), and inertia-gravity waves (W). A precursor to this study is that of TY, where a two-vertical-mode model was used to examine internal tide-balanced flow energy exchanges. Consequently, TY investigated energetic internal tide-balanced flow interactions while our investigation focused on NIW-balanced flow interactions.

Using the two vertical mode system, we examined the energy flow pathways between NIWs and balanced flows. Our detailed analysis of energy transfer between the different modes and across spatio-temporal scales of the modes allowed us to deduce the change in geostrophic turbulence phenomenology due to high-energy NIWs. In the absence of waves, the barotropic flow, which contains most of the balanced flow energy, would organize itself into domain filing coherent vortices. In contrast, high-energy waves transfer energy to the balanced flow and promotes a forward cascade of the barotropic balanced flow to smaller scales. Similarly, the balanced flow actively facilitates a forward cascade of waves' energy, transforming waves from large-scale NIWs to small-scale high-frequency inertia-gravity waves. Given that our model was completely two-dimensional, the forward energy cascade of wave and balanced flow is an intriguing feature. The overall energy flow pathways between the three modes is summarized in Fig. 13.

Although the long term dynamics consisting of high-frequency and small-scale waves and small-scale balanced flow would be inaccessible for existing asymptotic models that are derived for a few eddy turn over timescales, one might have anticipated the early time energy exchange between NIWs and balanced flow in our set up to agree with the results of the asymptotic predictions discussed in XV, WY, and RWY. Such an expectation is natural, since the baroclinic Eqs. (6b) and (6c) were used by Danioux et al. [17] and Thomas et al. [18] to derive the YBJ equation. Therefore, starting from our two-mode system (6), we could have proceeded along the same lines as XV and WY and derived an asymptotic model for the coupled evolution of NIWs and the barotropic balanced flow (ignoring the baroclinic balanced flow for simplicity). In such an asymptotic model, the wave field would evolve according the approximate YBJ equation while the balanced flow equation would consist of the barotropic vorticity and quadratic nonlinear wave-wave interaction terms. Most importantly, the asymptotic model derived starting from our two-vertical-mode equations would predict the same phenomenology as that discussed in RWY—NIWs would extract energy from balanced flow, their potential energy increasing due to direct extraction from the balanced flow while their kinetic energy being conserved.

For the specific case we examined in great detail with $\mathrm{Bu} = \mathrm{Ro}^2$, observe in Fig. 6(a) that the wave potential energy increases by about 5×10^{-4} within a few eddy turn over timescales. On decreasing the Burger number to $\mathrm{Bu} = \mathrm{Ro}^2/2$ (which corresponds to a higher baroclinic mode than the case where $\mathrm{Bu} = \mathrm{Ro}^2$) we find that wave potential energy increases by about 2×10^{-3} within a few eddy turn over timescales, as seen in Fig. 12(a). Furthermore, as discussed earlier, notice in Figs. 6(a) and 12(a) that the G-mode has insignificant energy and dissipation is negligible. Therefore if wave kinetic energy was conserved in our simulations, while other things remained unchanged, the barotropic mode's energy would have decreased by an amount equal to the increase in wave potential energy so as to conserve total energy of the system. Since $E_T = \mathrm{Ro}^2 = 0.01$ in our experiments, this

would imply that balanced flow would have lost approximately 5% and 20% energy within a few eddy turn over timescales in the cases shown in Figs. 6(a) and 12(a), respectively. Consequently, if wave kinetic energy was conserved, we would have concluded that NIWs extracted 5–20% of barotropic mode's energy. This is close to the magnitude of energy change predicted by coupled NIW-barotropic mode simulations discussed in XV and RWY—see Fig. 3 in XV, Fig. 8(a) in RWY and related discussions. Numerical experiments in XV predict about 5–10% loss in balanced energy while RWY predicts 10–20% balanced energy extraction by NIWs. However, contrary to the predictions of these asymptotic models, in our experiments NIWs kinetic energy was seen to decrease more than the increase in NIWs potential energy, resulting in net decrease in NIWs energy and corresponding increase in balanced energy. Consequently, our simulations point out that NIWs feed balanced energy in low balance-to-wave energy regimes and not the other way around.

Multiple restrictive assumptions used in the derivation of the asymptotic models contribute to their predictions differing from our findings. First, NIWs in the asymptotic models evolve according to the approximate YBJ equation—a model that conserves wave kinetic energy. In contrast, as seen in our numerical experiments, NIW kinetic energy is not conserved. Second, the balanced flow in these asymptotic models is an approximate Lagrangian mean flow derived based on two-timescale asymptotics. It is important to note that the Lagrangian mean flow in general is not in geostrophic balance [37,38]. As demonstrated using reduced models and direct numerical simulations in Thomas *et al.* [39], the Lagrangian mean flow can have a significant unbalanced component. The specific asymptotic derivations undertaken by XV and WY assume the Lagrangian mean flow to be in geostrophic balance, discarding unbalanced contributions. This approximate balanced flow is coupled with linear waves in the asymptotic models described above. The asymptotic assumptions involved in their derivation plays a key role in results leading to their prediction that NIWs directly extract energy from balanced flows via wave potential energy increase while wave kinetic energy remains constant. Our simulations of a nonasymptotic two-vertical-mode model—a parent model from which similar asymptotic models could be derived—stress the need to improve existing asymptotic models of NIW-balanced flow interactions so that their predictions agree with energy transfer directions predicted by parent models such as ours.

In spite of our reduced model being capable of capturing much more dynamics than the asymptotic NIW-balanced flow models, we once again remind the reader that our idealized two-dimensional model would miss important three-dimensional features. We therefore conclude by discussing how the phenomenology we found in two-dimensions would change in three dimensions. In three-dimensional hydrostatic Boussinesq equations, gravity waves have the dispersion relationship $\omega = \sqrt{1 + \mathrm{Bu}\, k^2/n^2}$ (k and n being the horizontal wavenumber and the baroclinic mode, respectively), implying that different horizontal wavenumbers and vertical modes, k and n, can be associated with the same frequency ω as long as they have the same k/n ratio. However, projecting the three-dimensional equations to a single baroclinic mode modifies the waves' dispersion relationship as $\omega = \sqrt{1 + \mathrm{Bu}\, k^2}$. Consequently, a forward energy cascade in two dimensions (resulting in the generation of larger k values with time) must necessarily generate higher frequencies in the wave field, as we observed in our simulations. In contrast, a forward wave energy cascade in three dimensions can take place by the concomitant generation of higher k and n values, without much change in the wave frequencies [40–42]. In other words, given a balanced flow, in three dimensions a forward cascade of wave energy can take place at more or less the same frequency as the original wave field, whereas a forward cascade in two dimensions is necessarily associated with the generation of higher frequency components. This forms the primary difference between the two-dimensional results reported in this paper and the three-dimensional results anticipated in similar set ups. Our preliminary three-dimensional simulations in similar set ups as described in this work, at small Rossby numbers and low balance-to-wave energy regimes, clearly show NIWs transferring energy to the balanced flow along with small-scale formation and dissipation of both wave and the balanced flow – phenomenology similar to that uncovered in this work. A major difference, however, is that the wave forward cascade takes place before significant

broadening of the frequency spectrum takes place. We expect to report on three-dimensional NIW-balanced flow interactions in the near-future.

[1] M. H. Alford, Internal swell generation: The spatial distribution of energy flux from the wind to mixed layer near-inertial motions, J. Phys. Oceanogr. **31**, 2359 (2001).

[2] M. Watanabe and T. Hibiya, Global estimates of the wind-induced energy flux to inertial motions in the surface mixed layer, Geophys. Res. Lett. **29**, 64–1 (2002).

[3] A. Gertz and D. N. Straub, Near-inertial oscillations and the damping of midlatitude gyres: A modeling study, J. Phys. Oceanogr. **39**, 2338 (2009).

[4] S. Taylor and D. Straub, Forced near-inertial motion and dissipation of low-frequency kinetic energy in a wind-driven channel flow, J. Phys. Oceanogr. **46**, 79 (2016).

[5] R. Barkan, K. B. Winters, and J. C. McWilliams, Stimulated imbalance and the enhancement of eddy kinetic energy dissipation by internal waves, J. Phys. Oceanogr. **47**, 181 (2017).

[6] L. N. Thomas and J. R. Taylor, Damping of inertial motions by parametric subharmonic instability in baroclinic currents, J. Fluid Mech. **743**, 280 (2014).

[7] T. A. Nagai, A. Tandon, E. Kunze, and A. Mahadevan, Spontaneous generation of near-inertial waves by the kuroshio front, J. Phys. Oceanogr. **45**, 2381 (2015).

[8] L. Thomas, On the effects of frontogenetic strain on symmetric instability and inertia-gravity waves, J. Fluid Mech. **711**, 620 (2012).

[9] C. J. Shakespeare and A. M. Hogg, The life cycle of spontaneously generated internal waves, J. Phys. Oceanogr. **48**, 343 (2018).

[10] E. Deusebio, A. Vallgren, and E. Lindborg, The route to dissipation in strongly stratified and rotating flows, J. Fluid Mech. **720**, 66 (2013).

[11] C. Herbert, R. Marino, D. Rosenberg, and A. Pouquet, Waves and vortices in the inverse cascade regime of stratified turbulence with or without rotation, J. Fluid Mech. **806**, 165 (2016).

[12] M. L. Waite, Random forcing of geostrophic motion in rotating stratified turbulence, Phys. Fluid **29**, 126602 (2017).

[13] W. R. Young and M. Ben Jelloul, Propagation of near-inertial oscillations through a geostrophic flow, J. Mar. Res. **55**, 735 (1997).

[14] J. H. Xie and J. Vanneste, A generalised-lagrangian-mean model of the interactions between near-inertial waves and mean flow, J. Fluid Mech. **774**, 143 (2015).

[15] G. L. Wagner and W. R. Young, A three-component model for the coupled evolution of near-inertial waves, quasigeostrophic flow and the near-inertial second harmonic, J. Fluid Mech. **802**, 806 (2016).

[16] C. B. Rocha, G. L. Wagner, and W. R. Young, Stimulated generation-extraction of energy from balanced flow by near-inertial waves, J. Fluid Mech. **847**, 417 (2018).

[17] E. Danioux, J. Vanneste, and O. Bühler, On the concentration of near-inertial waves in anticyclones, J. Fluid Mech. **773**, R2 (2015).

[18] J. Thomas, K. S. Smith, and O. Bühler, Near-inertial wave dispersion by geostrophic flows, J. Fluid Mech. **817**, 406 (2017).

[19] J. Thomas and R. Yamada, Geophysical turbulence dominated by inertia-gravity waves, J. Fluid Mech. **875**, 71 (2019).

[20] D. M. W. Frierson, A. J. Majda, and O. M. Pauluis, Large-scale dynamics of precipitation fronts in the tropical atmosphere: A novel relaxation limit, Commun. Math. Sci. **2**, 591 (2004).

[21] S. J. Benavides and A. Alexakis, Critical transitions in thin layer turbulence, J. Fluid Mech. **822**, 364 (2017).

[22] G. K. Vallis, *Atmospheric and Oceanic Fluid Dynamics* (Cambridge University Press, Cambridge, UK, 2006).

[23] J. C. McWilliams, Statistical properties of decaying geostrophic turbulence, J. Fluid Mech. **198**, 199 (1989).

[24] B. T. Nadiga, Nonlinear evolution of a baroclinic wave and imbalanced dissipation, J. Fluid Mech. **756**, 965 (2014).

[25] K. S. Smith and G. K. Vallis, The scales and equilibration of midocean eddies: Freely evolving flow, J. Phys. Oceanogr. **31**, 554 (2001).

[26] C. Wunsch, The vertical partition of oceanic horizontal kinetic energy and the spectrum of global variability, J. Phys. Oceanogr. **27**, 1770 (1997).

[27] V. D. Larichev and I. M. Held, Eddy amplitudes and fluxes in a homogeneous model of fully developed baroclinic instability, J. Phys. Oceanogr. **25**, 2285 (1995).

[28] R. Salmon, *Lectures on Geophysical Fluid Dynamics* (Oxford University Press, Oxford, 1978).

[29] A. D. D. Craik and S. Leibovich, A rational model for Langmuir circulations, J. Fluid Mech. **73**, 401 (1976).

[30] T. Humbert, S. Aumaitre, and B. Gallet, Wave-induced vortex recoil and nonlinear refraction, Phys. Rev. Fluids **2**, 094701 (2017).

[31] S. Leibovich, On wave-current interaction theories of Langmuir circulations, J. Fluid Mech. **99**, 715 (1980).

[32] E. A. D'Asaro, C. C. Eriksen, M. A. Levine, P. Niiler, C. A. Paulson, and P. van Meurs, Upper ocean inertial currents forced by a strong storm. part I: Data and comparisons with linear theory, J. Phys. Oceanogr. **25**, 2909 (1995).

[33] D. -K. Lee and P. P. Niiler, The inertial chimney: The near-inertial energy drainage from the ocean surface to the deep layer, J. Geophys. Res. **103**, 7579 (1998).

[34] S. Elipot, R. Lumpkin, and G. Prieto, Modification of inertial oscillations by the mesoscale eddy field, J. Geophys. Res. **115**, C09010 (2010).

[35] H. A. Kafiabad and P. Bartello, Spontaneous imbalance in the nonhydrostatic boussinesq equations, J. Fluid Mech. **847**, 614 (2018).

[36] A. Alexakis and L. Biferale, Cascades and transitions in turbulent flows, Phys. Rep. **767-769**, 1 (2018).

[37] O. Bühler, *Waves and Mean Flows* (Cambridge University Press, Cambridge, 2014).

[38] A. D. D. Craik, *Wave Interactions and Fluid Flows* (Cambridge University Press, Cambridge, 1985).

[39] J. Thomas, O. Bühler, and K. S. Smith, Wave-induced mean flows in rotating shallow water with uniform potential vorticity, J. Fluid Mech. **839**, 408 (2018).

[40] P. Bartello, Geostrophic adjustment and inverse cascades in rotating stratified turbulence, J. Atmos. Sci. **52**, 4410 (1995).

[41] H. Kafiabad, M. A. C. Savva, and J. Vanneste, Diffusion of inertia-gravity waves by geostrophic turbulence, J. Fluid Mech. **869**, R7 (2019).

[42] M. P. Lelong and J. J. Riley, Internal wave-vortical mode interactions in strongly stratified flows, J. Fluid Mech. **232**, 1 (1991).